Publ. Astron. Soc. Japan (2018) 70 (3), 45 (1–10)
doi: 10.1093/pasj/psy035
Advance Access Publication Date: 2018 April 18

Exploring the origin of broad-band emissions of Mrk 501 with a two-zone model

Maichang Lei,[1,2,3,*] Chuyuan Yang,[1,2,3] Jiancheng Wang,[1,2,3] and Xiaolin Yang[1,2,3]

[1]Yunnan Observatories, Chinese Academy of Sciences, Kunming 650011, China
[2]Key Laboratory for the Structure and Evolution of Celestial Objects, Chinese Academy of Sciences, Kunming 650011, China
[3]Center for Astronomical Mega-Science, Chinese Academy of Sciences, 20A Datun Road, Chaoyang District, Beijing, 100012, China

*E-mail: maichanglei83@ynao.ac.cn

Received 2017 June 26; Accepted 2018 March 6

Abstract

We propose a two-zone synchrotron self-Compton (SSC) model, including an inner gamma-ray emitting region with spherical shape and a conical radio emitting region located at the extended jet, to alleviate the long-standing "bulk Lorentz factor crisis" in blazars. In this model, the spectral energy distributions (SEDs) of blazars are produced by considering the gamma-ray emitting region inverse Compton scattering of both the synchrotron photons itself and the ambient photons from the radio emitting region. Applying the model to Mrk 501, we obtain that the radio emitting region has a comoving length of ∼0.15 pc and is located at sub-parsec scale from the central engine by modeling the radio data; the flux of the Compton scattering of the ambient photons is so low that it can be neglected safely. The characteristic hard gamma-ray spectrum can be explained by the superposition of two SSC processes, and the model can approximately explain the very high energy (VHE) data. The insights into the spectral shape and the inter-band correlations under the flaring state will provide us with a diagnostic for the bulk Lorentz factor of radio emitting region, where the low and upper limits of 8 and 15 are preferred, and for the two-zone SSC model itself. In addition, our two-zone SSC model shows that the gamma-ray emitting region creates flare on the timescale of merely a few hours, and the long time outbursts more likely originate from the extended radio emitting region.

Key words: BL Lacertae objects: individual (Markarian 501) — galaxies: active — galaxies: jets — radiation mechanisms: general

1 Introduction

Blazars are extreme radio-loud active galactic nuclei (AGNs) and are subdivided into BL Lacertae objects (BL Lacs) and flat-spectrum radio quasars (FSRQs). BL Lacs show featureless optical spectra. Typically, the spectral energy distribution (SED) of a blazar shows a double-humped morphology in the ν–νF_ν representation (Fossati et al. 1998), and is dominated by non-thermal emissions from the jet, which closely aligns with the line of sight, and the emission is therefore strongly Doppler boosted (Urry & Padovani 1995). The low-energy hump of the SED, spanning from radio to X-rays, is widely believed

to be the synchrotron radiation of the relativistic electrons; while the high-energy component is attributed to Compton scattering of soft photons either produced by synchrotron process (synchrotron self-Compton, SSC; Maraschi et al. 1992; Bloom & Marscher 1996; Mastichiadis & Kirk 1997) or contributed by external radiation fields (external radiation Compton, ERC; Dermer et al. 1992; Dermer & Schlickeiser 1993; Sikora et al. 1994; Ghisellini et al. 1998; Böttcher 2007). Alternatively, hadronic processes may also play an important role in producing high-energy emissions (Aharonian 2000; Mücke & Protheroe 2001; Mücke et al. 2003; Yan & Zhang 2015). In terms of the synchrotron peak frequency, $\nu_{\rm peak}$, blazars can be classified as low-peaked (LBLs, $\nu_{\rm peak} \lesssim 10^{14}$ Hz), intermediate-peaked (IBLs, $10^{14} < \nu_{\rm peak} \lesssim 10^{15}$ Hz), and high-peaked (HBLs, $\nu_{\rm peak} > 10^{15}$ Hz) blazars (Abdo et al. 2010).

The multi-frequency emissions and the physical properties of the emission region of a blazar are generally explored based on one-zone homogeneous SSC models, but the radio data fail to be explained thus. The radio emission is commonly thought to be contributed by the extended jet components. In such a framework, a high bulk Lorentz factor is usually necessary, $\Gamma_\gamma \gtrsim 25$,[1] to explain the short gamma-ray variability (Aharonian et al. 2007; Ghisellini & Tavecchio 2008; Albert et al. 2007; Ackermann et al. 2016). Finke, Dermer, and Böttcher (2008) applied a bulk Lorentz factor larger than 100 to explain the observed SED of PKS 2155 −304. Higher bulk Lorentz factors of from 30 up to 100 are invoked to reproduce the SEDs of Mrk 421 and PKS 1424+240 (Horan et al. 2009; Aleksić et al. 2012, 2014; Zhu et al. 2016). Kakuwa et al. (2015) fitted the quasi-simultaneous data of Mrk 421 and Mrk 501 to get bulk Lorentz factors of 35 and 31, respectively.

However, the observations by the Very Long Baseline Interferometry (VLBI) and/or Very Long Baseline Array (VLBA) showed that the jet moves outward only at subluminal speed (bulk speed $\lesssim$1 c) on about parsec scales (Piner et al. 1999, 2009; Tiet et al. 2012), and a fraction of radio core components of Mrk 501 even appear to be stationary (Edwards & Piner 2002). For several HBLs, the bulk Lorentz factors of the parsec-scale jets were found to be relatively low, ranging from ∼3 to 4 (Giroletti et al. 2004, 2006; Wu et al. 2007; Piner et al. 2008). The VLBA images of six HBLs gave an apparent speed of jet bulk motion of $<2c$ near the core (Piner et al. 2010). Piner and Edwards (2014) performed VLBI observations of 20 HBLs to constrain their brightness temperatures as $\sim 2 \times 10^{10}$ K, ruling out the need for any relativistic beaming effects. Such dramatic deviation of the bulk Lorentz factors between the model and observations is the so-called "bulk Lorentz factor crisis" (Henri & Saugé 2006).

An extensive multi-frequency observation of Mrk 501 was carried out over a time period of 4.5 months in 2009, and obtained a very hard intrinsic γ-ray spectrum at the Fermi energy band, which is difficult to explain with a one-zone SSC model (Abdo et al. 2011). Shukla et al. (2015) proposed a multi-zone SSC model to explain the complex broad-band spectra and flux variability of Mrk 501, but their model did not place a constraint on the location of the radio emission and did not consider the interaction between two emission regions. Ahnen et al. (2017) presented a detailed study of Mrk 501 based on the data from 2009 and concluded that the SEDs associated separately with two flares, in which the very hard spectra appear at soft X-rays and γ-rays.

In this paper, we present a two-zone SSC model in order to study the origin of the multi-band emissions of Mrk 501 and the possible interactions between two emission regions, which are referred to as gamma-ray and radio emitting regions. In this model, an external radiation field from the radio emitting region provides the seed photons of Compton scattering in the gamma-ray region, its contribution from such process to gamma-rays should be considered. In section 2, we describe the two-zone SSC model and numerical methods, and apply them to Mrk 501 in section 3. The discussion and conclusions are presented in section 4.

2 Model setup

In this section, we set up a two-zone SSC model based on a conical leptonic jet. In figure 1, we present the schematic diagram of the geometrical structure of the two emission regions. The gamma-ray emitting region, with

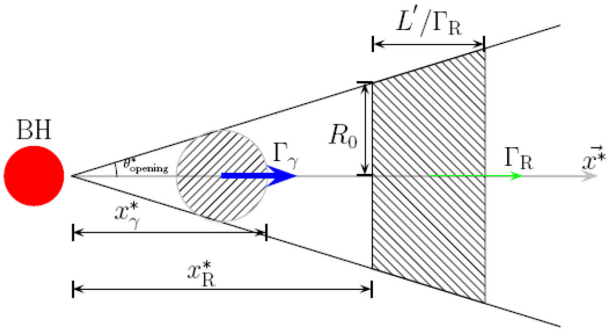

Fig. 1. A schematic picture of a two-zone jet structure, where the relative location of the gamma-ray and the radio emitting regions with different bulk Lorentz factors, Γ_γ and $\Gamma_{\rm R}$, is shown. The two emission regions are depicted by shaded areas, moving outward along the x^*-axis. The length L' is measured in the comoving frame of the radio region, and the remaining parameters denoted in the figure are defined in the stationary frame of a black hole (BH). (Color online)

[1] Throughout this paper, the quantity X relating to the gamma-ray and the radio emitting regions is denoted as X_γ and $X_{\rm R}$, respectively.

an assumed spherical configuration and larger Γ_γ, contributes variable emissions in both the X-ray and very high energy (VHE, $E_\gamma \gtrsim 100\,\mathrm{GeV}$) bands via SSC and/or ERC processes. In contrast, the radio emitting region, with an assumed conical configuration and smaller Γ_R, produces steady radio and GeV radiations. The radio emitting region is constructed following the approach of Potter and Cotter (2012) and Zheng and Yang (2016), in which an amount of the leptonic energy E^*_R is injected instantaneously into the base of the truncated cone; subsequently, the non-thermal electron population evolves into an extended region of size $\Gamma_\mathrm{R} L'$, where L' is the length measured in the comoving frame.[2] $\theta^*_\mathrm{opening}$ is the half-opening angle of the jet; both emission regions are moving outward along the x^*-axis, and their locations are assigned by the quantities of x^*_γ and x^*_R. Detailed physical properties for two emission regions, as well as ERC process between them, are presented as follows. Throughout the paper, the Hubble constant is taken as $H_0 = 71\,\mathrm{km\,s^{-1}\,Mpc^{-1}}$, and the matter energy density and dimensionless cosmological constant are $\Omega_\mathrm{m} = 0.27$ and $\Omega_\Lambda = 0.73$, respectively.

2.1 Gamma-ray emitting region

In the model, we simplify the gamma-ray emitting region into a blob, where the comoving size r_γ can be inferred from the observed minimum variability timescale $t_{\gamma,\mathrm{var}}$ as $r_\gamma \simeq c\delta_{\gamma,\mathrm{D}} t_{\gamma,\mathrm{var}}/(1+z)$, where z is the redshift; $\delta_{\gamma,\mathrm{D}}$ is the Doppler factor, which relates to the bulk Lorentz factor $\delta_{\gamma,\mathrm{D}} = [\Gamma_\gamma(1-\beta_\gamma\cos\theta_\mathrm{v})]^{-1}$ and the dimensionless bulk velocity $\beta_\gamma = [1-\Gamma_\gamma^{-2}]^{1/2}$. The blob is filled with a tangled magnetic field B_γ and isotropically non-thermal electron populations. We assume that the electrons reach the steady state under acceleration, injection, escape, and radiative losses; this is consistent with the fact that the resulting energy spectrum is the average of flux over a certain timescale. The distribution of the non-thermal electrons is described by two power-law functions in the form

$$n''_\mathrm{e}(\gamma'') = \begin{cases} n_0 \gamma''^{-p_1} & \gamma''_\mathrm{min} \le \gamma'' \le \gamma''_\mathrm{br} \\ n_0 \gamma''^{-p_2} \gamma''^{\,p_2-p_1}_\mathrm{br} & \gamma''_\mathrm{br} < \gamma'' \le \gamma''_\mathrm{max}, \end{cases} \tag{1}$$

where n_0 is the normalization, and p_1 and p_2 are the spectral indices below and above the break energy γ''_br.

2.2 Extended radio emitting region

The radio emitting region has a bulk Lorentz factor Γ_R that corresponds to a Doppler factor $\delta_{\mathrm{R,D}} = [\Gamma_\mathrm{R}(1-\beta_\mathrm{R}\cos\theta_\mathrm{v})]^{-1}$ and bulk velocity β_R. When it travels down the jet, its radius changes continuously as

$$R(x') = R_0 + x' \tan\theta'_\mathrm{opening}, \tag{2}$$

where θ'_opening is the jet half-opening angle, which relates to $\theta^*_\mathrm{opening}$ via $\tan\theta'_\mathrm{opening} = \Gamma_\mathrm{R}\tan\theta^*_\mathrm{opening}$. Initially, the injected electrons satisfy a single power-law distribution with a cut-off energy γ'_cut, e.g., $N'_\mathrm{e}(\gamma') = A\gamma'^{-\alpha}\exp(-\gamma'/\gamma'_\mathrm{cut})$, in the range from γ'_min to γ'_max. These energetic electrons are injected immediately into a narrow region at the base of the truncated cone. Because the various energy losses are very weak, and the total energy is reasonably thought to be conserved, we obtain

$$R_0 = \left[\frac{2\mu_0}{\pi B_\mathrm{R}^2}\frac{A_\mathrm{eq}E^*_\mathrm{R}}{\Gamma_\mathrm{R}^2(1+A_\mathrm{eq})}\right]^{1/2}, \tag{3}$$

$$A = \frac{E^*_\mathrm{R}}{m_\mathrm{e}c^2\Gamma_\mathrm{R}^2}\frac{2-\alpha}{(\gamma'^{2-\alpha}_\mathrm{cut} - \gamma'^{2-\alpha}_\mathrm{min})(1+A_\mathrm{eq})}, \tag{4}$$

where $\mu_0 = 4\pi$ is the magnetic permeability, A_eq is the equipartition fraction, and B_R is the comoving magnetic field strength.

Provided that the conservation of the magnetic energy flux along the jet, the magnetic field can be expressed as $B(x') = B_\mathrm{R}R_0/R(x')$, which describes a pure toroidal field that is perpendicular to the jet axis. After injections, the electron population will evolve when an electron slab of width 1 cm passes through a section of width dx' along the jet in the fluid frame,[3] according to the equation

$$N'_\mathrm{e}(\gamma'; x'+dx') = N'_\mathrm{e}(\gamma'; x') - \frac{P'_\mathrm{tot}(\gamma'; x', dx')}{c\gamma' m_\mathrm{e}c^2}, \tag{5}$$

where $P'_\mathrm{tot} = P'_\mathrm{syn} + P'_\mathrm{ssc}$ is the total power emitted by electrons with energy γ' within a section of width dx' via synchrotron and SSC processes. The electron distribution thus follows

$$N'_\mathrm{e}(\gamma'; x') = \frac{A\tilde{}N'_\mathrm{e}(\gamma'; x')}{N'_\mathrm{e}(\gamma'; x'=x'_0)}\gamma'^{-\alpha}\exp\left(-\frac{\gamma'}{\gamma'_\mathrm{cut}}\right). \tag{6}$$

The synchrotron emissivity from electrons located at x' within a jet section of width dx' is given by

$$j'_\mathrm{syn}(\epsilon'; x') = \frac{\sqrt{3}e^3 B(x')}{h\pi R(x')^2}\int_1^\infty d\gamma' N'_\mathrm{e}(\gamma'; x') R(X) \times\{1-\exp[-k_\epsilon(\epsilon'; x')dx]\}, \tag{7}$$

[2] The notations Q', Q'', and Q^* refer to the quantities in the radio emitting and the gamma-ray emitting regions as well as in the stationary frame of the black hole, while the others are the observer's quantities.

[3] The two notations used here are such that $X(x; y) \equiv \partial X/\partial x$ and $X(x; y_1, y_2) \equiv \partial X/\partial x$, where y, y_1, and y_2 are the parameters, specifically, y and y_1 are related to x', while y_2 is related to $\mathrm{d}x'$.

where e is the fundamental charge, h is the Planck's constant. $R(X)$ is given by Finke, Dermer, and Böttcher (2008). k_ϵ is the opacity given by equation (25) in Potter and Cotter (2012). Accordingly, the energy density of the synchrotron emission is given by

$$u'_{\rm syn}(\epsilon';x') \simeq j'_{\rm syn}(\epsilon';x')\frac{R(x')}{c}. \tag{8}$$

Consequently, the total synchrotron emissivity from the radio emitting region is given by

$$J'_{\rm syn}(\epsilon') = \sum_{x'} j'_{\rm syn}(\epsilon';x',dx')\exp[-\tau'_{\rm tot}(\epsilon';x')], \tag{9}$$

where $\tau'_{\rm tot}$ is the total synchrotron opacity.

2.3 ERC process between two emission regions

Because the gamma-ray emitting region is assumed to have a larger bulk Lorentz factor than the radio emitting one, corresponding to the decelerated jet (Georganopoulos & Kazanas 2003; Wang et al. 2004), the contribution from the ERC process to overall SED of the source should be considered in the comoving frame of the gamma-ray emitting region. Considering an isotropic electron distribution, the comoving Compton spectral luminosity is written as

$$\epsilon''_{\rm s}L''_{\rm c}(\epsilon''_{\rm s},\Omega''_{\rm s}) = \frac{3c\sigma_{\rm T}}{32\pi}\epsilon''^2_{\rm s}\int_0^{2\pi}d\phi''\int_{-1}^{\mu''_{\rm max}}d\mu'' \times\int_0^{\epsilon''_{\rm hi}}d\epsilon''\frac{u''(\epsilon'',\Omega'')}{\epsilon''^2}\int_{\gamma''_{\rm low}}^{\infty}d\gamma''\frac{N''_{\rm e}(\gamma'')}{\gamma''^2}\Xi, \tag{10}$$

where $\epsilon''_{\rm hi}$, $\gamma''_{\rm low}$, and Ξ are given in Dermer et al. (2009), and $u''(\epsilon'',\Omega'')$ is the energy density of the external radiation field given in the following. In an SSC situation, equation (10) will reduce to equation (9) presented in Finke, Dermer, and Böttcher (2008).

In the stationary frame of the black hole (BH), the starting point $x^*_{\rm R}$ of the radio emitting region and the end point x^*_γ of the gamma-ray emitting region can be expressed as

$$x^*_{\rm R} = R_0/\tan\theta^*_{\rm opening}, \tag{11}$$

$$x^*_\gamma = r_\gamma/\tan\theta^*_{\rm opening} + \Delta x^*_{\rm coll}, \tag{12}$$

where $\Delta x^*_{\rm coll} = ct_{\gamma,{\rm var}}\Gamma_\gamma\delta_{\gamma,{\rm D}}/(1+z) = \Gamma_\gamma r_\gamma$. $x'_{\rm R}$ and x'_γ, measured in the comoving frame of the radio emitting region, are obtained through the Lorentz transformations $x'_{\rm R} = x^*_{\rm R}/\Gamma_{\rm R}$ and $x'_\gamma = x^*_\gamma/\Gamma_{\rm R}$. The emissivity of the synchrotron emission can be derived, and this procedure relies on the relative locations of these two quantities.

In this study, we only focus on the situation where the two emission regions are not in contact, with $x'_\gamma < x'_{\rm R}$. Therefore, the energy density of the synchrotron emission is given approximately by

$$u'(\epsilon') \simeq \frac{J'_{\rm syn}(\epsilon')}{4\pi(x'_{\rm R}-x'_\gamma+\Delta x^*_{\rm coll}/\Gamma_{\rm R})^2c}. \tag{13}$$

We obtain the energy density in the frame of the gamma-ray emitting region by a simple Lorentz transformation,

$$u''(\epsilon'',\Omega'') = \frac{u'(\epsilon')}{4\pi[\Gamma_{\rm rel}(1+\beta_{\rm rel}\mu'')]^3}, \tag{14}$$

$$\Gamma_{\rm rel} = \Gamma_\gamma\Gamma_{\rm R}(1-\beta_\gamma\beta_{\rm R}), \tag{15}$$

where

$$\epsilon'' = \Gamma_{\rm rel}\epsilon'(1-\beta_{\rm rel}\mu'), \tag{16}$$

$$\mu' = (\mu''-\beta_{\rm rel})/(1-\beta_{\rm rel}\mu''), \tag{17}$$

$$\beta_{\rm rel} = \frac{\beta_\gamma-\beta_{\rm R}}{1-\beta_\gamma\beta_{\rm R}}. \tag{18}$$

2.4 Numerical implementation

For the radio emitting region, the electrons in a section of plasma of width dx' will lose their energy by radiation when they move along the jet. The evolution of the energy distribution is governed by the kinetic equation, i.e., equation (5), similar to the solution for the Fokker–Plank equation. Its discrete form is

$$N'_{\rm e}(\gamma'_{\rm i};x'_{\rm j}) = N'_{\rm e}(\gamma'_{\rm i};x'_{\rm j-1}) - \frac{P'_{\rm tot}(\gamma'_{\rm i};x'_{\rm j-1})}{c\gamma'_{\rm i}m_{\rm e}c^2}. \tag{19}$$

Once the initial spectral shape of the electron distribution is known, equation (19) can be solved easily. In order to ensure the right-hand side of equation (19) has no negative solutions, we need the condition of $dx' < c\delta t'_{\rm c}$ to hold, where $\delta t'_{\rm c} \simeq \gamma' m_{\rm e}c^2/P'_{\rm syn}$ is the electron synchrotron cooling timescale. In calculations, we take $x'_0 = 100$ cm and the length grid is expressed as $x'_{\rm i} = x'_{\rm i-1} + dx'$. Moreover, the energy grid is given by

$$\delta\xi = \frac{\log(\xi_{\rm max})-\log(\xi_{\rm min})}{\rm m}, \tag{20}$$

where ξ is related to electron energies γ'', γ' or photon energies ϵ'', ϵ'. $\xi_{\rm max}$ and $\xi_{\rm min}$ are the maximum and minimum energies of the particles, and m is the meshpoints number.

As mentioned above, the radio emitting region is constructed following the approach of Potter and Cotter (2012). However, several aspects in the present model differ substantially from the primordial one: first, our calculation employs dimensionless quantities about electron and photon energies, because the calculation employs dimensionless quantities that means it is convenient to use it to calculate the ERC processes; secondly, in calculation of synchrotron and SSC spectra, we apply the formulae presented by Finke, Dermer, and Böttcher (2008) and/or Dermer et al. (2009). In the two-zone model proposed here, the gamma-ray emitting region is assumed to take up the entire cross-section of the jet in the stationary frame of the BH; the distance from the central engine is thus determined by $x^*_\gamma \simeq r_\gamma / \tan\theta^*_{\rm opening}$.

3 Application to Mrk 501

During the period from 2009 March 15 to August 1, a coordinated multi-frequency campaign was performed by the Fermi Large Area Telescope (Fermi-LAT, Atwood et al. 2009) and other instruments, with excellent temporal and energy coverage (Abdo et al. 2011). The average SED shows a concave and very hard gamma-ray spectrum, with photon index $\Gamma = 1.1 \pm 0.2$ (Neronov et al. 2012). Such a hard spectrum could be affected by the strong γ-ray flares which occurred during the multi-frequency observation. In practice, it has been shown by Abdo et al. (2011) that the flux level of the high-energy tail of Fermi-LAT observations is really compatible with the flux of the VERITAS flare, in which in the VHE flux increases by a factor of 10. In contrast, the flux level of the low-energy end is in good agreement with the MAGIC and VERITAS flux when the source was in quiescence. Abdo et al. (2011) performed SED modeling as well as parameter analysis, using only the low-state data in ahigh-energy bump, even through the SED also includes the observation of the VERITAS flare. We therefore call it a "quiescent-state" SED. In this paper, we also incorporate the low-state data from long-term observations of Fermi and ARGO-YBJ instruments (Bartoli et al. 2012); these data match with low-state observations of MAGIC and VERTAS well, implying that the average quiescent-state SED is typical for Mrk 501 when it was in the inactive stage (see figure 3). More recently, Ahnen et al. (2017) also performed an extensive multi-frequency study of Mrk 501 spanning the same time coverage as Abdo et al. (2011), and presented two broad-band SEDs corresponding respectively to two prominent flaring events, denoted as MJD 54952 and MJD 54973. Both SEDs show the variations of apparent flux and spectral shape compared to the quiescent state. The first flare has large VHE flux change in sub-hour timescales, while the second one has a smaller flux change and longer timescales. We call the two episodes "flaring states." In the following, we will explore the origin of these multi-frequency emissions and the properties of the emission regions. For clarity, we divide the source into quiescent and flaring states to study the physical properties.

In order to reduce free parameters of the model, we adopt $\theta^*_{\rm opening} = 3^\circ$ and a viewing angle $\theta_{\rm v} = 2^\circ$, and assume a priori that the bulk Lorentz factor of the gamma-ray emitting region is $\Gamma_\gamma = 25$, which is commonly required to fit the flaring SED (Albert et al. 2007; Böttcher et al. 2008; Tavecchio et al. 2010; Acciari et al. 2011; Mankuzhiyil et al. 2012; Kakuwa et al. 2015). In both emission regions, the maximum electron Lorentz factors are fixed at 5×10^7, while for the radio emitting region the minimum Lorentz factor is fixed at unity. The TeV data have been corrected for the extragalactic background light (EBL) absorption based on the model by Franceschini, Rodighiero, and Vaccari (2008).

Owing to serious synchrotron self-absorption for the inner gamma-ray emitting region, the observed radio emission mainly arises from the extended radio emitting region. The distance between γ-ray and radio core emission is related to the apparent time delay by (Pushkarev et al. 2010)

$$\delta t_{\rm delay} = \frac{\Delta x^*(1+z)}{\Gamma_{\rm rel}\delta_{\rm rel,D}\beta_{\rm rel}c}, \tag{21}$$

where Δx^* is the interval between the emission regions, $\Gamma_{\rm rel}$ is the relative bulk Lorentz factor, and $\delta_{\rm rel,D}$ is the corresponding Doppler factor. We assume that the γ-rays above tens of GeV arise from the gamma-ray emitting region, while the radio emitting region could produce GeV photons.

3.1 Quiescent state

We investigate the quiescent state SED, beginning with modeling the flat radio spectrum of Mrk 501, as shown in figure 2. The procedure mainly depends on seven quantities, which are divided into two groups: the first one consists of the total injection power $P^*_{\rm R} = cE^*_{\rm R}$, the bulk Lorentz factor $\Gamma_{\rm R}$, the cut-off energy of the electron distribution $\gamma'_{\rm cut}$, and the equipartition fraction $A_{\rm eq}$; the second one includes the spectral index of the electron distribution α, the length L', and the magnetic field strength $B_{\rm R}$ at the base of the truncated cone. As the first step of the modeling process, we provide some initial values for two parameters in the second group based on physical considerations or past investigations. Specifically, α is set to be 2.2, wherein the standard Fermi second-order accelerations are assumed to energize the thermal particles; $B_{\rm R}$ is set as 0.05 Gs, which

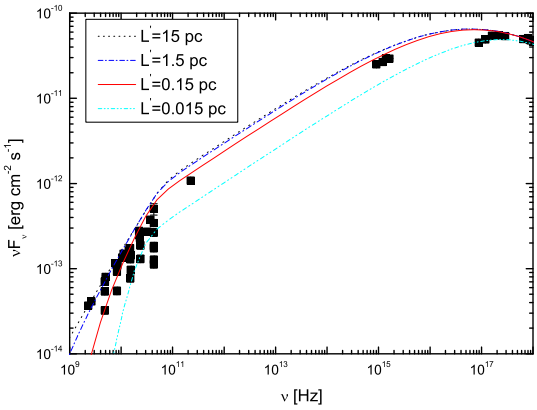

Fig. 2. Fitting of the flat radio spectrum of Mrk 501 through changing the length of the radio emitting region. The preferable value of $L' = 0.15$ pc is shown with the red solid line, and is used in the following figures. (Color online)

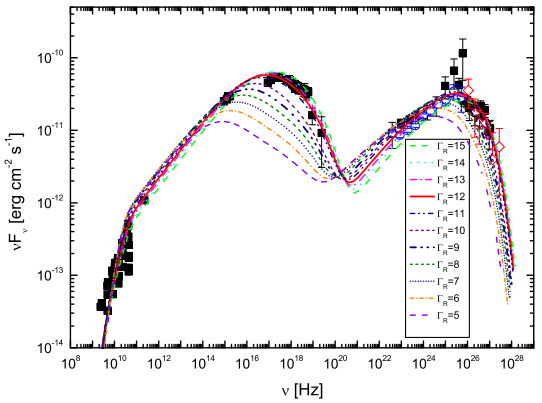

Fig. 3. Model fit to the quiescent state of Mrk 501 through changing the bulk Lorentz factor of the radio emitting region as labeled, in which $\Gamma_R = 12$ is shown with a solid line, which represents the best fit to the multi-frequency data. The black squares represent the data points taken in the multifrequency campaign from 2009 March 15 to August 1, and the empty blue circles and red diamonds represent the Fermi and ARGO-YBJ long-term observations, respectively. (Color online)

Table 1. Parameters for the radio emitting region of Mrk 501.

Description	P_j^* [10^{44} erg s^{-1}]	A_{eq} [10^{-3}]	α	γ'_{cut} [10^5]	B_R [G]	Γ_R
Quiescent state	1.6	1.5	2.2	28	0.021	12
Flaring state	0.9	6	2.1	0.93	0.021	8

roughly approaches the one obtained in the previous multi-frequency investigations (Abdo et al. 2011; Bartoli et al. 2012; Finke 2013; Peng et al. 2014; Shukla et al. 2015; Kakuwa et al. 2015; Aleksić et al. 2015; Furniss et al. 2015; Aliu et al. 2016). For L', without loss of generality, it can be fixed at 1 kpc in this case. Next, we carry out the SED modeling to the quiescent state SED without including the radio data; this modeling will determine the parameters of the first group. Thirdly, we fine-tune all of the parameters except L'; the resulting model parameters are presented in table 1, denoted as "Quiescent state". Subsequently, we read just the value of L' to obtain a best fit for the flat radio spectrum. In figure 2 only four curves are shown, corresponding to different L' values, i.e., 0.015 pc, 0.15 pc, 1.5 pc, and 15 pc. From the figure, it is clear that when L' is 1.5 pc or more, the fitting to the radio data is nearly similar; when L' is less than 0.015 pc, the lower radio flux and serious synchrotron self-absorption reproduce the radio up to optical spectra. In comparison, only $L' = 0.15$ pc gives a best fit as far as the radio data are concerned, corresponding to a distance from the central engine of $x_R^* \simeq 0.2$ pc. The model obtains $R_0 = 2.4 \times 10^{16}$ cm. Hereafter, the length L' is fixed at 0.15 pc.

As mentioned before, the bulk Lorentz factor of the radio emitting region located at the extended regions of the jet is of the order of a few. Keeping other parameters constant but changing Γ_R from 5 to 15, we perform the modeling to the quiescent SED using only the radio emitting region, and the results are presented in figure 3. Here several points need to be emphasized: for $\Gamma_R = 15$, because the positions of synchrotron and SSC emission peaks move to higher energies, the model curve apparently deviates from the GeV data, implying that the bulk Lorentz factor of the radio emitting region cannot be more than 15 in a one-zone SSC scenario; when Γ_R increases from 11 to 15, the radio emitting model can fit all-wavelength data; if Γ_R is less than 11, the model can fit the high-energy bump and the radio to ultraviolet (UV) spectrum, but fails to fit to the X-ray data. It is noted that when Γ_R takes the value 8, the radio to UV spectra and the left-hand side of the high-energy bump can be produced by the radio emission region, but the X-ray spectrum and the right-hand side of the high-energy bump must be produced by another emission region.

The quiescent state SED is also fitted by the two-zone SSC model, in which we take Γ_R to be 12, but decrease the cut-off energy γ'_{cut}. At this time, $x_R^* \simeq 0.2$ pc; the model also gives an R_0 of 3.5×10^{16} cm, and provides an upper limit to the gamma-ray emitting region of $t^u_{\gamma,var} \simeq \frac{R_0(1+z)}{c\delta_{\gamma,D}} \approx 11.8$ hr. Thus we take $t_{\gamma,var}$ equal to 12 hr as the variability timescale of the gamma-ray emitting region, and keep the parameters of the radio emitting region constant, as presented in table 1, as we carry out the SED modeling again. The results are presented in figure 4, and the parameters of the gamma-ray emitting region are listed in table 2. In a two-zone scenario, the radio to UV band and the GeV photons are from the radio emitting region, while the X-ray and VHE photons are provided by the gamma-ray emitting region. In contrast, the ERC flux is significantly low. The superposition of two regions results in the total quiescent state SED, and the hard GeV γ-ray spectrum can be approximately

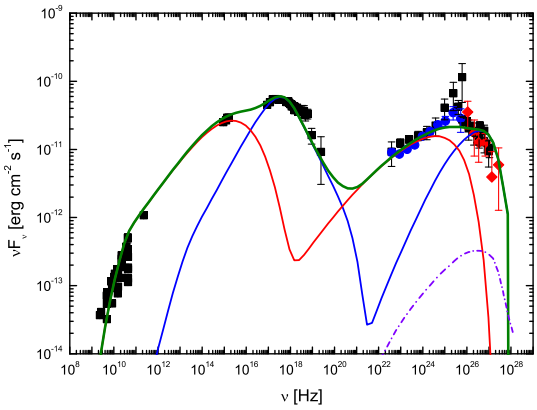

Fig. 4. Model fitting for quiescent state SED in the framework of two-zone SSC scenarios, in which the red and blue lines represent SSC emissions from radio and gamma-ray emitting regions, respectively; the ERC contribution is denoted by the purple dash–dotted line, and the green line is the total model curve. Here we take the variability timescale of the gamma-ray emitting region $t_{\rm var}$ equal to 12 hr. (Color online)

produced. The contribution of synchrotron processes from two regions creates a shallow trough between UV and X-ray bands, which is consistent with the data. While the combination from two SSC processes constitutes a platform, it contrasts with the peaked shape data distribution. We remark that our two-zone model is likely to provide an explanation to the origin of the quiescent state SED; the high-energy tail of the Fermi-LAT observations, as stated previously, may be affected by some VHE flares. As well as fundamental model parameters, the table also presents the total magnetic and electron power, $P^*_{\gamma,\rm B}$ and $P^*_{\gamma,\rm e}$, calculated via $P^*_{\gamma,\rm i} = (4/3)\pi r_\gamma^3 \Gamma_\gamma^2 \int u'_{\rm i} dV'$, where $i = $ e, B, and $u'_{\rm i}$ is the related energy density. The result shows that in a gamma-ray emitting region the matter energy is about three orders of magnitude than the magnetic energy, this indicates that at the scale of the gamma-ray emitting region lies, where the magnetic energy has been seriously transformed to the bulk kinetic energy of the jet, and ruling out the magnetic reconnection as an underlying acceleration mechanism for relativistic electrons within the emission region.

3.2 Flaring state

Now we analyze the properties of the broad-band SEDs during two flaring states in 2009 May. Their SEDs are not strictly simultaneous, and the observed minimum variability timescales for two VHE flares are $t_{\gamma,\rm var} \lesssim 0.25$ hr and $t_{\gamma,\rm var} \lesssim 1$ d (Ahnen et al. 2017). Thus, we perform flaring state SED modeling adopting only the intra-hour variability timescales. The SEDs of two flares significantly differ from those in the quiescent state, in which the peaks of synchrotron and VHE γ-ray emissions move to higher energies and higher flux appear. Compared to the quiescent state, the flaring state spectra show an apparent division; this spectral shape is difficult to reconcile with a one-zone SSC scenario. Such disagreements are the main motivation for this paper. Although $\Gamma_{\rm R}$ can be 8 or 12, similarly good SED modeling can be obtained (when $\Gamma_{\rm R} > 12$, the SED moves toward the right, thus the model cannot fit the radio data); here we only take the lower limit of 8 for the SED modeling. Meanwhile, given the difference between the quiescent and the flaring state SEDs, mainly in radio and GeV bands, the modeling parameters relating to the radio emitting region are re-adjusted. The SED modeling results are shown in figure 5, and the model parameters of the radio emitting region are incorporated into table 1, denoted as "Flaring state"; the parameters of the gamma-ray emitting region are listed in table 3. For the intra-hour γ-ray variability, the distance interval is very large, leading to relatively low ambient photon energy density; the ERC contribution is too low to be shown in figures. The new parameters of both emission regions are substantially different from the original ones. Particularly, for the radio emitting region, the model obtains relatively low values for $P^*_{\rm j}$, α, and $\gamma'_{\rm cut}$, as well as a higher $A_{\rm eq}$. In the gamma-ray emitting region, as the $t_{\gamma,\rm var}$ changes, the variation in the model parameters is the same as in the quiescent state. From figure 5, a strong correlation between X-ray and VHE bands can be seen; the correlation of radio and GeV γ-ray emissions will be slightly weak, due to the low flux and narrow observed energy band, which could be a characteristic of a two-zone SSC model. Similarly, the model results in $x^*_{\rm R} \simeq 0.4$ pc and $R_0 \approx 7.1 \times 10^{16}$ cm, corresponding to $t^{\rm u}_{\gamma,\rm var} \approx 24$ hr, indicating that the γ-ray outburst with an observed variability timescale of more than one day does not originate from the gamma-ray emitting region. It should be emphasized here that, due to the complexity of the implicit physical processes as well as the data gathered with different time spans for different telescope instruments, our

Table 2. Parameters for the gamma-ray emitting region during quiescent state.

n_0 [cm^{-3}]	$\gamma''_{\rm min}$	$\gamma''_{\rm br}$	p_1	p_2	B_γ [Gs]	$P^*_{\gamma,\rm B}$ [erg s^{-1}]	$P^*_{\gamma,\rm e}$ [erg s^{-1}]
17	8.6×10^3	1.3×10^6	1.81	4.3	0.0034	3.4×10^{40}	5.6×10^{43}

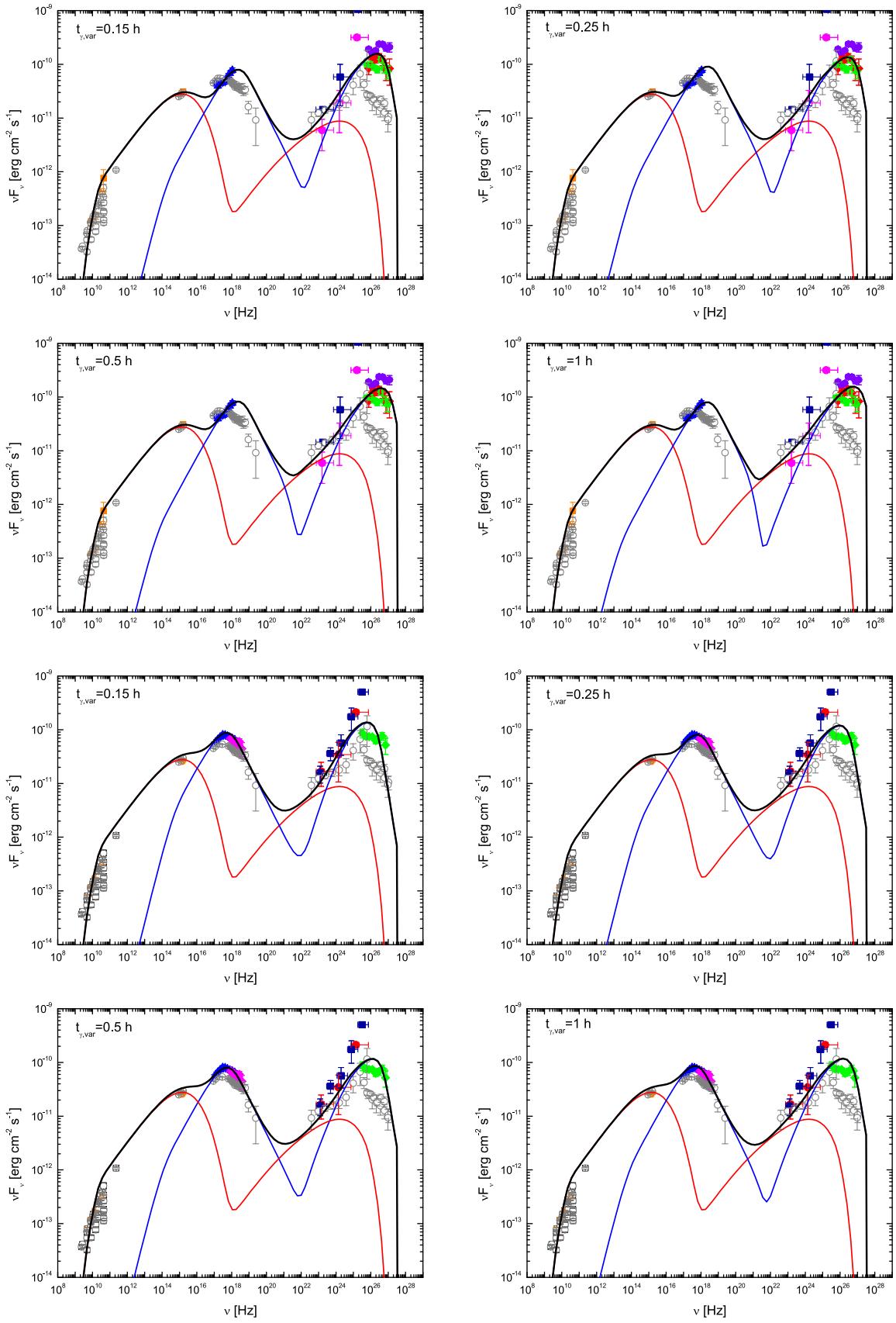

Fig. 5. Model fitting for flaring state SEDs in the framework of two-zone SSC scenarios (upper four panels: MJD 54952; lower four panals: MJD 54973). The descriptions for each curve are the same as figure 4, while the black solid line is the total model curve. (Color online)

Table 3. Parameters of the gamma-ray emitting region during the flaring states.

Parameters	MJD 54952				MJD 54973			
	$t_{\gamma,\mathrm{var}} = 0.15$ hr	$t_{\gamma,\mathrm{var}} = 0.25$ hr	$t_{\gamma,\mathrm{var}} = 0.5$ hr	$t_{\gamma,\mathrm{var}} = 1$ hr	$t_{\gamma,\mathrm{var}} = 0.15$ hr	$t_{\gamma,\mathrm{var}} = 0.25$ hr	$t_{\gamma,\mathrm{var}} = 0.5$ hr	$t_{\gamma,\mathrm{var}} = 1$ hr
n_0 [cm^{-3}]	4.7×10^4	1.9×10^4	8×10^3	3.3×10^3	3.2×10^4	1.5×10^4	5.5×10^3	2×10^3
γ''_{min}	8.6×10^3	8.6×10^3	8.6×10^3	8.6×10^3	8.6×10^3	8.6×10^3	8.6×10^3	8.6×10^3
γ''_{br}	9.7×10^5	1.2×10^6	1.8×10^6	2.8×10^6	2.8×10^5	4.3×10^5	5.8×10^5	7.4×10^5
p_1	1.81	1.81	1.81	1.81	1.81	1.81	1.81	1.81
p_2	4.3	4.3	4.3	4.3	4.3	4.3	4.3	4.3
B_γ [Gs]	0.064	0.044	0.018	0.0075	0.17	0.086	0.042	0.022
$P^*_{\gamma,\mathrm{B}}$ [erg s^{-1}]	1.9×10^{39}	2.5×10^{39}	1.7×10^{39}	1.2×10^{39}	1.3×10^{40}	9.5×10^{39}	9.1×10^{39}	1×10^{40}
$P^*_{\gamma,\mathrm{e}}$ [erg s^{-1}]	2.2×10^{43}	2.6×10^{43}	5×10^{43}	9.3×10^{43}	9.9×10^{42}	1.5×10^{43}	2.4×10^{43}	3.8×10^{43}

model only approximately explains the VHE data; hence the derived conclusions need to be taken within the model constraints.

4 Discussion and conclusions

A two-zone SSC model was established in this paper to alleviate the "bulk Lorentz factor crisis" in blazars, in which the radio emitting region can naturally reproduce the flat radio spectrum which is usually neglected in the context of one-zone leptonic model. The model also analyzes the interaction between the emission regions. We apply the model to study the origin of the broad-band SEDs of Mrk 501, and obtain a comoving length of the radio emitting region of 0.15 pc, corresponding to a distance from the central engine of 0.2 pc for the quiescent state and either 0.2 or 0.44 pc for the flaring state. Undoubtedly, due to the complexity of the VHE emissions, our model only provides an approximate explanation for VHE data points. Piner, Pant, and Edwards (2010) presented VLBA images of six TeV blazars and obtained $\Gamma_{\mathrm{R}} < (\Gamma_\gamma)^{1/2}$. For a typical Lorentz factor, $\Gamma_\gamma \sim 25$, this means that $\Gamma_{\mathrm{R}} \lesssim 5$ and $\Gamma_{\mathrm{R}} \lesssim 3.5$ at 10^5 and 10^6 R_{s} (R_{s} is the Schwarzschild radius of the BH). Piner and Edwards (2014) imposed the modest limit of $\Gamma_{\mathrm{R}} \gtrsim 2$, given the fact that there is no detection of a counter jet. In contrast, our modeling of Mrk 501 requires a Γ_{R} larger than 8, but less than 15, which is still less than the Γ_γ required for modeling high-energy emissions in short-term TeV flares. This implies that the jet could be decelerated while moving outward. Actually, if the radiation is dominated by anisotropic external radiation, the Compton drag effect will cause a leptonic jet to recoil (Sikora et al. 1996; Ghisellini & Tavecchio 2010). Whether the ambient radiation field from the radio emitting region is the main agent for decelerating the gamma-ray emitting region or not will be analyzed in a subsequent work.

We divide the SEDs of Mrk 501 obtained during the multi-frequency campaigns in 2009 into quiescent and flaring states. Specifically, the quiescent state SED is presented by Abdo et al. (2011), and two flaring state SEDs are given by Ahnen et al. (2017). The SED modeling results limit the Γ_{R} to a broader range, from 8 up to 15. Given that radio emitting components generally show low apparent speed, we take $\Gamma_{\mathrm{R}} = 8$ as a lower limit. In such case, both the quiescent and flaring state SEDs need to invoke two emission regions to reproduce multi-frequency emissions; the VHE flare will correlate tightly with the X-ray activity, and the radio burst will accompany GeV activity, which also agrees with steep decline of the spectral shape in soft X-rays. Therefore, the investigations of spectral shape and inter-band correlation will provide us with a diagnostic for Γ_{R} and the origin of the VHE flare. Under the two-zone SSC model, the variability timescale of the inner gamma-ray emitting region is limited to a few hours. If that were true, γ-ray activities with timescales above a few hours must occur in the radio emitting region, where certain mechanisms will lead particle acceleration and injections. In such a situation, the emissions from radio up to VHE γ-rays will originate from a single emission region, and the correlated variabilities at all energy bands, in principle, could be observed. At this time, the radiative output is dominated by the radio emitting region, and a larger bulk Lorentz factor could occur. By those arguments, there are two crude criteria by which to judge whether the one-zone or two-zone model is used for exploring the origin of the multi-frequency emissions in blazars.

First, if the high-energy activities with variability timescales of the orders of 10 hours or even longer are detected, we can apply a one-zone SSC model to describe the overall multi-band emissions, in which the emission region could have a larger bulk Lorentz factor, and the correlated variability will appear in the whole electromagnetic spectrum.

Secondly, if the correlated variability only appears in both the X-ray and VHE energy bands, the two-zone SSC model could be a better choice. The VLBA/VLBI observations on the bulk Lorentz factor of the radio emitting regions will provide further support.

Finally, we present our main results, as follows.

(1) We apply a two-zone SSC model to study the origin of the multi-frequency emissions of Mrk 501, in which the contribution from the ERC process can be neglected safely.
(2) The two-zone SSC model is used to explain the hard gamma-ray spectrum, which is approximately produced by the superposition of two SSC spectra from radio and gamma-ray emitting regions.
(3) The SED modeling to Mrk 501 during the quiescent state constrains the length of the radio-emitting region to be about 0.15 pc, and the location of the radio base to be on sub-parsec scales.
(4) The bulk Lorentz factor of the radio emitting region of Mrk 501 has a broader range, from 8 to 15. An unambiguous determination depends upon detailed spectral shape and inter-band correlation, which could provide us with a diagnostic to the two-zone SSC model.

Acknowledgments

We thank the anonymous referee for very constructive comments that have helped us improve the presentation of the paper. We thank David Paneque and Chen Songzhan for sending us the observed data sets used in this paper, and Jian-Fu Zhang for useful discussions and comments. We acknowledge the financial supports from the National Natural Science Foundation of China 11661161010, 11573060, 11673060 and the Strategic Priority Research Program, the Emergence of Cosmological Structures of the Chinese Academy of Sciences, Grant No. XDB09000000.

References

Abdo, A. A., et al. 2010, ApJ, 716, 30
Abdo, A. A., et al. 2011, ApJ, 727, 129
Acciari, V. A., et al. 2011, ApJ, 729, 2
Ackermann, M., et al. 2016, ApJ, 824, L20
Aharonian, F., et al. 2007, ApJ, 664, L71
Aharonian, F. A. 2000, New Astron., 5, 377
Ahnen, M. L., et al. 2017, A&A, 603, A31
Albert, J., et al. 2007, ApJ, 669, 862
Aleksić, J., et al. 2012, A&A, 542, A100
Aleksić, J., et al. 2014, A&A, 567, A135
Aleksić, J., et al. 2015, A&A, 573, A50
Aliu, E., et al. 2016, A&A, 594, A76
Atwood, W. B., et al. 2009, ApJ, 697, 1071
Bartoli, B., et al. 2012, ApJ, 758, 2
Bloom, S. D., & Marscher, A. P. 1996, ApJ, 461, 657
Böttcher, M. 2007, Ap&SS, 307, 69
Böttcher, M., Dermer, C. D., & Finke, J. D. 2008, ApJ, 679, L9
Dermer, C. D., Finke, J. D., Krug, H., & Böttcher, M. 2009, ApJ, 692, 32
Dermer, C. D., & Schlickeiser, R. 1993, ApJ, 416, 458
Dermer, C. D., Schlickeiser, R., & Mastichiadis, A. 1992, A&A, 256, L27
Edwards, P. G., & Piner, B. G. 2002, ApJ, 579, L67
Finke, J. D. 2013, ApJ, 763, 134
Finke, J. D., Dermer, C. D., & Böttcher, M. 2008, ApJ, 686, 181
Fossati, G., Maraschi, L., Celotti, A., Comastri, A., & Ghisellini, G. 1998, MNRAS, 299, 433
Franceschini, A., Rodighiero, G., & Vaccari, M. 2008, A&A, 487, 837
Furniss, A., et al. 2015, ApJ, 812, 65
Georganopoulos, M., & Kazanas, D. 2003, ApJ, 594, L27
Ghisellini, G., Celotti, A., Fossati, G., Maraschi, L., & Comastri, A. 1998, MNRAS, 301, 451
Ghisellini, G., & Tavecchio, F. 2008, MNRAS, 386, L28
Ghisellini, G., & Tavecchio, F. 2010, MNRAS, 409, L79
Giroletti, M., Giovannini, G., Taylor, G. B., & Falomo, R. 2004, ApJ, 613, 752
Giroletti, M., Giovannini, G., Taylor, G. B., & Falomo, R. 2006, ApJ, 646, 801
Henri, G., & Saugé, L. 2006, ApJ, 640, 185
Horan, D., et al. 2009, ApJ, 695, 596
Kakuwa, J., Toma, K., Asano, K., Kusunose, M., & Takahara, F. 2015, MNRAS, 449, 551
Mankuzhiyil, N., Ansoldi, S., Persic, M., Rivers, E., Rothschild, R., & Tavecchio, F. 2012, ApJ, 753, 154
Maraschi, L., Ghisellini, G., & Celotti, A. 1992, ApJ, 397, L5
Mastichiadis, A., & Kirk, J. G. 1997, A&A, 320, 19
Mücke, A., & Protheroe, R. J. 2001, Astroparticle Phys., 15, 121
Mücke, A., Protheroe, R. J., Engel, R., Rachen, J. P., & Stanev, T. 2003, Astroparticle Phys., 18, 593
Neronov, A., Semikoz, D., & Taylor, A. M. 2012, A&A, 541, A31
Peng, Y., Yan, D., & Zhang, L. 2014, MNRAS, 442, 2357
Piner, B. G., & Edwards, P. G. 2014, ApJ, 797, 25
Piner, B. G., Pant, N., & Edwards, P. G. 2008, ApJ, 678, 64
Piner, B. G., Pant, N., & Edwards, P. G. 2010, ApJ, 723, 1150
Piner, B. G., Pant, N., Edwards, P. G., & Wiik, K. 2009, ApJ, 690, L31
Piner, B. G., Unwin, S. C., Wehrle, A. E., Edwards, P. G., Fey, A. L., & Kingham, K. A. 1999, ApJ, 525, 176
Potter, W. J., & Cotter, G. 2012, MNRAS, 423, 756
Pushkarev, A. B., Kovalev, Y. Y., & Lister, M. L. 2010, ApJ, 722, L7
Shukla, A., et al. 2015, ApJ, 798, 2
Sikora, M., Begelman, M. C., & Rees, M. J. 1994, ApJ, 421, 153
Sikora, M., Sol, H., Begelman, M. C., & Madejski, G. M. 1996, MNRAS, 280, 781
Tavecchio, F., Ghisellini, G., Ghirlanda, G., Foschini, L., & Maraschi, L. 2010, MNRAS, 401, 1570
Tiet, V. C., Piner, B. G., & Edwards, P. G. 2012, arXiv:1205.2399
Urry, C. M., & Padovani, P. 1995, PASP, 107, 803
Wang, J., Li, H., & Xue, L. 2004, ApJ, 617, 113
Wu, Z., Jiang, D. R., Gu, M., & Liu, Y. 2007, A&A, 466, 63
Yan, D., & Zhang, L. 2015, MNRAS, 447, 2810
Zheng, Y. G., & Yang, C. Y. 2016, MNRAS, 457, 3535
Zhu, Q., Yan, D., Zhang, P., Yin, Q.-Q., Zhang, L., & Zhang, S.-N. 2016, MNRAS, 463, 4481